

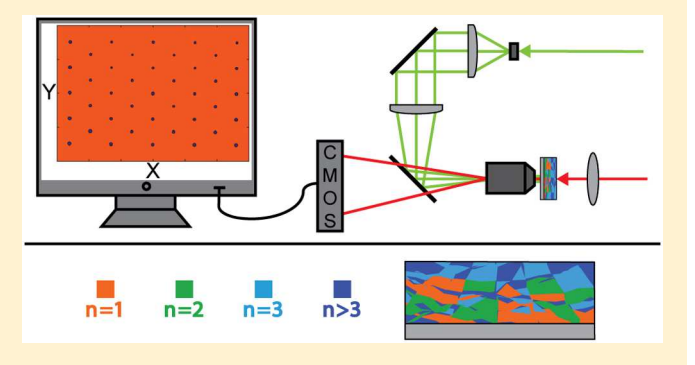
Imaging Excited State Dynamics in Layered 2D Perovskites with Transient Absorption Microscopy

Published as part of The Journal of Physical Chemistry virtual special issue "Time-Resolved Microscopy". Olivia F. Williams,[†] Ninghao Zhou,[†] Jun Hu,[†] Zhenyu Ouyang,[†] Amar Kumbhar,[‡] Wei You,[†] and Andrew M. Moran*,†

[†]Department of Chemistry, [‡]Chapel Hill Analytical and Nanofabrication Laboratory, University of North Carolina at Chapel Hill, Chapel Hill, North Carolina 27599, United States

Supporting Information

ABSTRACT: Two-dimensional (2D) hybrid perovskites are generating broad scientific interest because of their potential for use in photovoltaics and microcavity lasers. It has recently been demonstrated that mixtures of quantum wells with different thicknesses can be assembled in films with heterogeneous quantum well distributions. Large (small) quantum wells are concentrated at the air side (substrate side) of the films, thereby promoting directional energy and/or electron transfer. However, profiles of the quantum well concentrations have not been directly measured throughout the full thicknesses of the films. Similarly, the lateral motions of the excitations in these systems are not well-characterized.



In this work, we perform focused ion beam milling tests to establish quantum well concentrations as a function of depth in layered 2D perovskite films. In addition, transient absorption microscopy is used to investigate carrier diffusion and two-body recombination processes. Comparisons of the layered films with phase-pure single crystals reveal that diffusion is suppressed by grain boundaries in the films, which in turn promotes two-body recombination. Similar behaviors were previously observed in bulk perovskite films and single crystals. These studies suggest that the morphology of the film, rather than the identity of the material, is the primary factor that governs the two-body recombination dynamics. Enhancement of the two-body recombination processes is desirable for applications such as microcavity lasers.

I. INTRODUCTION

The extraordinary optoelectronic and photovoltaic properties of conventional perovskites¹⁻³ have renewed interest in twodimensional (2D) hybrid perovskite quantum wells as a more stable alternative. 4-6 Perovskite quantum wells are generally described by the chemical formula $A_2B_{n-1}M_nY_{3n+1}$, where A is a bulky organic cation, B is a smaller cation, M is metal cation, and Y is a halide. The A cation serves as an insulator that surrounds portions of the conductive perovskite lattice, thereby confining excitations to the conductive layers. These materials initially drew attention because of fundamental interest in their electronic structures;⁷⁻¹⁰ however, such confinement effects may be leveraged in these 2D systems to optimize resonance frequencies, binding energies, and oscillator strengths for optoelectronic applications. 11-16 Photoexcited electron-hole pairs are quantum-confined in these systems because the thicknesses of the quantum wells are smaller than the Bohr radii of the excitons.⁷ The general behaviors predicted with simple analytical models (e.g., 2D hydrogen atom)¹⁷⁻¹⁹ are realized in 2D perovskites, where the binding energies and oscillator strengths far exceed those found in 3D perovskites.

It has recently been shown that 2D perovskite quantum wells with different sizes can be suspended in thin films with a gradient in the exciton absorption frequency. 12,13,20 As shown in Figure 1, quantum wells with the smallest thicknesses and highest-frequency resonances are concentrated near the glass substrate, whereas those with the largest thicknesses are found near the air side of the film. ^{20–22} The systems considered in this work are described by the formula $(PEA)_2(MA)_{n-1}[Pb_nI_{3n+1}]$, where MA is methylammonium and PEA is phenethylammonium. The band gaps decrease as the index, n, increases; excitonic resonances for n = 1-6quantum wells span the 515-705 nm wavelength range. Whereas energy transfer dominates the sub-200 ps time scale, 21 the energy levels of the quantum wells are arranged such that hole transfer may occur from the air to glass sides of the film at later times.²⁰

In this work, we establish the gradients in quantum well concentrations throughout the full thickness of the film, as well

Received: September 17, 2019 Revised: November 13, 2019 Published: November 15, 2019



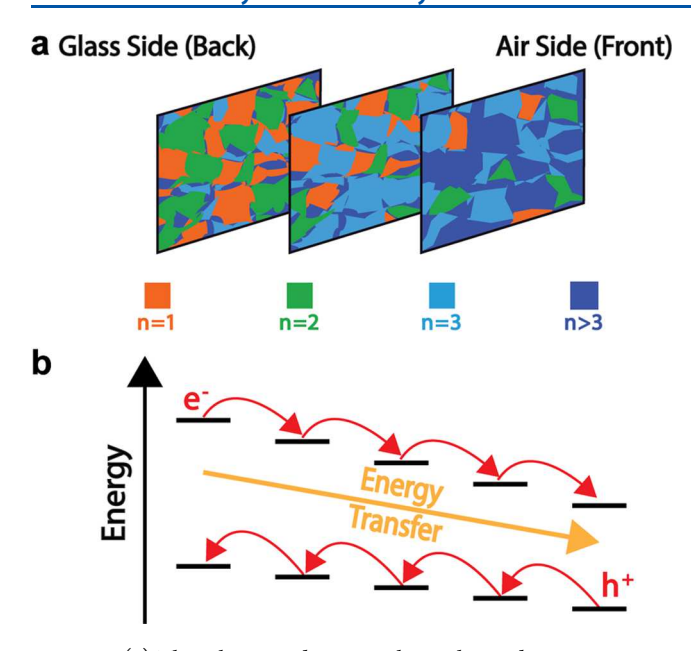


Figure 1. (a) The schematic depiction shows the gradient in quantum well concentrations throughout a layered perovskite film. The smallest quantum wells are most highly concentrated on the glass side of the film, whereas the thickest quantum wells are most prevalent on the air side. (b) Excitonic resonances of the quantum wells decrease as the thickness increases, enabling a downhill energy transfer cascade. Electron transfer may proceed in the same direction as energy transfer, while holes are expected to move to higher energy states.

as the orientations of transition dipoles. Further, we image the dynamics of electronic excitations in layered 2D perovskite quantum wells with transient absorption microscopy (TAM).^{23–30} Layered films and phase-pure single crystals are compared to establish diffusivities and two-body recombination rates. This approach takes inspiration from a previous study in which carrier diffusion was shown to be most prominent in 3D perovskite single crystals, whereas two-body recombination dominated in films.²⁸ These data suggest that disordered grains and/or grain boundaries promote two-body recombination by confining excitations to smaller volumes. The finding of enhanced two-body relaxation rates in the present layered 2D perovskite films may suggest a general behavior, wherein the morphology is of comparable importance to the intrinsic properties of the semiconductor in deciding the nature of the dynamics.

The photoinduced relaxation scheme associated with these particular layered perovskite systems was previously mapped out using conventional transient absorption techniques.²¹ These data suggest that the large transition dipoles (>10 D),¹⁰ short inter-quantum well distances (0.9 nm),⁹ and staggered band gaps combine to promote energy transfer into the thickest quantum wells in less than 300 ps.²¹ This interpretation of the dynamics is supported by response function-based fits of transient absorption spectra in a basis of single excitons and biexcitons.^{21,22} Consistent with the large exciton binding energies found in these systems,³¹ our data show that electron transfer between quantum wells is not responsible for the dynamic red shift in signal intensity observed in the visible wavelength range on this time scale.^{21,22} In addition, we find that 40–50% of excitations relax by way of "dark" decay pathways, which may represent exciton dissociation at "layer edge states".³²

II. EXPERIMENTAL METHODS

IIA. Sample Preparation. Two-dimensional perovskite films were prepared on the basis of previously reported methods. Phenethylammonium iodide (PEAI) and dimethylformamide (DMF) were obtained from Sigma-Aldrich, lead iodide was obtained from Alfa Aesar, and methylammonium iodide (MAI) was obtained from Solaronix. All materials were used without further purification.

ITO-coated coverslips (SPI; 30–60 Ω resistivity, 22 × 22 mm) were cleaned via sonication for 20 min in a series of four solvents: Contrex AP glassware detergent in deionized water, deionized water, acetone, and 2-propanol. Substrates were dried in a stream of nitrogen gas following the 2-propanol wash and then cleaned via UV-ozone for 15 min at 150 °C. Clean slides were preheated at 100 °C for ~15 min immediately before film deposition. FTO slides (Sigma; ~13 Ω/sq , ~2 × 2 cm) were used as substrates for focused ion beam (FIB) and scanning electron microscopy (SEM) studies and were prepared in the same manner as the ITO-coated coverslips, excluding treatment with UV-ozone.

The 2D perovskites employed in these studies were made from a blend of nominally $N_{\rm max}=2$ and $N_{\rm max}=3$ precursors (here we use the notation from ref 21). The $N_{\rm max}=2$ solution, containing a 2:1:2 molar ratio of PEAI, MAI, and PbI $_2$, respectively, was prepared by dissolving PEAI (0.288 g), MAI (0.092 g), and PbI $_2$ (0.533 g) in DMF (2 mL). The $N_{\rm max}=3$ solution, with a 2:2:3 molar ratio of PEAI, MAI, and PbI $_2$, respectively, was prepared by dissolving PEAI (0.288 g), MAI (0.184 g), and PbI $_2$ (0.800 g) in DMF (2 mL). The blended precursor was obtained by combining 150 μ L of $N_{\rm max}=2$ solution, 400 μ L of $N_{\rm max}=3$ solution, and 200 μ L of DMF. The resulting precursor blend was then filtered using a 0.2 μ m PTFE syringe filter to remove any particulates.

Films were prepared by spin coating 150 μ L of filtered precursor blend at 3000 rpm for 20 s (1500 rpm/second acceleration) onto the clean, preheated substrate. Spin coating procedures were conducted within a glovebox to promote smoother morphology of the resulting films.

For 2D perovskite crystals, the synthesis of *n*-butylammonium iodide (BAI) and MAI were conducted on the basis of previously reported methods.²² Briefly, unstabilized hydroiodic acid (HI; 57 wt % in water; obtained from Sigma-Aldrich) was purified using tributyl phosphate (0.36 M) in chloroform. Purified HI was then reacted with stoichiometric quantities of *n*-butylamine or methylamine (both from Sigma-Aldrich). The crude product was obtained under reduced pressure and recrystallized in ethanol. The final product was washed with ethyl ether and dried under vacuum at 60 °C.

Synthesis of $(BA)_2(MA)_{n-1}Pb_nI_{3n+1}$ (n=1,2, and 3) crystals was based on a previously reported procedure, with some modifications. For n=1, a slow cooling method was used.³³ Briefly, stoichiometric quantities of PbI_2 (Alfa Aesar) and n-butylamine were dissolved in a minimum volume of HI (57 wt % with stabilizer; Alfa Aesar) at 95 °C. Once fully dissolved, the solution was slowly cooled to room temperature at a rate of 1 °C/h. The resultant orange crystals were filtered and dried under vacuum overnight. For n=2 and n=3, a slow evaporation method was used.³⁴ Briefly, stoichiometric quantities of PbI_2 , BAI, and MAI were dissolved in a mixed solvent of HI (57 wt % with stabilizer) and H_3PO_2 (Sigma-Aldrich) with a 5.88:1 ratio at 60 °C. Once fully dissolved, the solution was evaporated slowly overnight. The crystals were

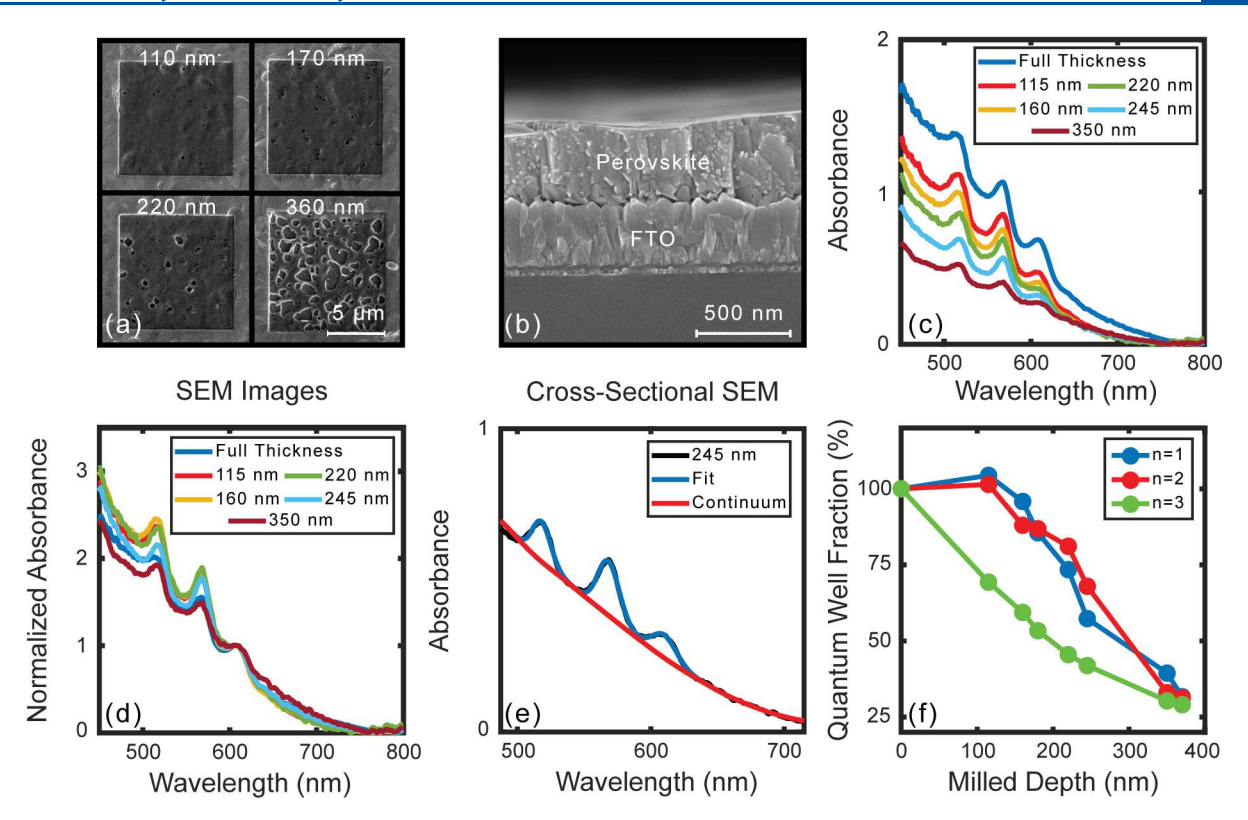


Figure 2. (a) Representative SEM images of four milled regions with indicated depths, as determined by AFM. (b) The cross-sectional SEM image shows the full thickness of the layered perovskite film. (c) Average absorbance line shapes are given for full thickness films and milled regions. The average line shapes are calculated from milled regions on multiple samples with depths that differ by no more than 20 nm. See Figures S1–S4 for complete characterization of individual samples. (d) Average absorbance spectra are normalized to the n = 3 exciton resonance at 610 nm. (e) The representative fit of the continuum (red) and total absorbance line shape (blue) is shown for 245 nm milled region. The black line represents the experimental measurement. (f) The average change in quantum well concentration is shown as a function of milling depths.

collected and dried with filter paper. Finally, the crystals were dried under vacuum overnight.

Microsized flakes were isolated and transferred to microscope slides via mechanical exfoliation. Briefly, the perovskite crystals were exfoliated by Scotch tape (3M) for 5–10 times and then transferred to a precleaned glass microscope slide. Crystals were selected for measurements on the basis of absorbance and fluorescence spectra obtained using a Craic 20/30 PV microspectrophotometer (MSP). From the n=3 synthesis, a small amount of n=4 phase was also isolated and studied in this work.

IIB. Transient Absorption Microscopy. The TAM instrument used in this work was described in a previous publication.²⁸ Briefly, all experiments are conducted with a 45 fs, 4 mJ Coherent Libra laser system with a 1 kHz repetition rate. Continuum pump and probe pulses are produced by focusing 1.5 mJ of the 800 nm fundamental beam into a 2 m long tube filled with argon gas to induce continuum generation. The continuum is then divided into pump and probe beams with a 70:30 beam splitter. The two laser beams are passed through all-reflective 4F setups, which are based on 1200 g/mm gratings and 20 cm focal length mirrors. Motorized slits at the Fourier planes are used to filter the desired portions of the pump and probe spectra. The spectrally filtered pulses have 250 fs durations and 6 nm widths. The bandwidths of the pump pulses are set equal to 6 nm in all experiments. The bandwidths of the probe pulses are set to 6 nm for measurements of transient absorption spectra and 12

nm for studies of spot width dynamics to maximize dynamic range. Pulse energies are controlled with neutral density filters.

A diffractive optic (Holoeye) is used to split the pump into 41 beams, which are then focused onto the sample with a microscope objective (Olympus). The infinity-corrected microscope objective has a magnification of 40x, a numerical aperture of 0.95, and a working distance of 0.18 mm. The tube lens located between the objective and the detector is also infinity-corrected and has an 18 cm focal length. The FWHM spot size of each pump beam is 1.0 μ m on the sample surface. The probe beam, which has a fluence of approximately 15 μ J/ cm² at the sample, is focused to a spot size of 150 μ m from the opposite side of the microscope objective using a 25 cm focal length lens. The probe intensity varies by less than 12% at the various pump spots because the probe diameter is larger than the field-of-view. Such small differences in the probe intensity are irrelevant in transient absorption experiments because differential absorption is independent of the probe intensity.

The CMOS detector is 12-bit with a 1024×1280 array of pixels and 915 Hz maximum frame rate (Phantom Miro C110). The array is synchronized with our 1 kHz laser system in a 480×640 pixel binning mode. An optical chopper, which is placed in the path of the pump beam, cycles the instrument between the pump-on, S_1 , and pump-off, S_2 , conditions at 500 Hz. Differential absorption is then computed as $\Delta A = \log(S_1) - \log(S_2)$. Each differential absorption image is averaged over a total of 100 images in a single scan of the delay line. The delay line is scanned 20–30 times during each experiment. We do

not observe variation in the signal profiles for data acquisition times up to 90 min.

IIC. Focused Ion Beam Milling. Focused ion beam (FIB) milling experiments³⁵ are conducted with an FEI Helios 600 Nanolab Dual Beam System for both sample milling and SEM image collection. Prior to FIB experiments, layered perovskite films are coated with ∼3 nm of Au/Pd via sputtering to prevent excessive charging within the electron microscope.

Perovskite films are patterned with four 10 μ m \times 10 μ m squares that are milled to depths indicated in Figure 2 (Figures S1–S4) by accelerated Ga⁺ ions (30 kV). Ion beam current is varied between 28 and 93 pA to achieve well-defined milled areas while maintaining reasonable patterning times. SEM images are obtained using an 86 pA electron beam current and 5.00 kV accelerating voltage. Cross-sectional SEM images are obtained under the same conditions.

Exact thicknesses of the milled areas are determined with an Asylum Research MFP3D atomic force microscope (AFM) equipped with a silicon tip (see Figures S5–S8 for AFM depth profiles). The linear absorbances of the full thickness films and milled areas are obtained using the MSP equipped with an Ultrafluar 40× objective. All spectra are collected using a 6.2 μ m × 6.2 μ m aperture to sufficiently average over the heterogeneity of the film within the milled regions. Integration times between 300 and 400 ms are used, depending on sample thickness, to achieve high signal quality; all absorbance profiles were collected 300 times and averaged.

III. RESULTS AND DISCUSSION

IIIA. Concentration Distributions and Orientations of Quantum Wells. In previous work, fluorescence spectra acquired with light incident on opposite sides of layered perovskite films demonstrated that the smallest and largest quantum wells are primarily concentrated near the glass and air sides of the films, respectively. Notably, these measurements do not provide profiles of particular quantum well concentrations as a function of depth. For example, fluorescence spectra cannot determine if the smallest quantum wells are homogeneously distributed under a layer of bulk material, or if the average sizes of the quantum wells steadily increase from the glass to air sides of the film.

In order to directly observe and quantify the layered morphology suggested by fluorescence measurements, linear absorbance spectra were measured as a function of depth using FIB milling experiments. FIB techniques and accelerated Ga+ ions were used to mill perovskite films because of the highly tunable and controlled strength of the ion beam, which allows for milling to a variety of specific depths without compromising the integrity of the remaining sample. Due to subtle differences in the interaction of Ga⁺ ions with the sample, the same parameters used for the FIB may result in slightly different depth profiles, as observed in the AFM data. After patterning the samples and determining the milled depths (Figure 2a), the concentrations of the quantum wells could be extracted from linear absorbance spectra of the full thickness and milled regions (Figure 2c). Subtraction of the broad absorbance line shape associated with continuum states is first accomplished using an algorithm designed to separate resonance Raman signals and fluorescence signals.³⁶ After the broad component of the absorbance line shape is removed, the narrow exciton resonances of the quantum wells are fit with a sum of weighted Gaussians,

$$\sigma(\omega) = \sum_{n=1}^{3} c_n \exp\left[-4\ln(2)\frac{(\omega - \omega_n)^2}{d_n^2}\right]$$
 (1)

where c_n is the magnitude, ω_n is the exciton resonance frequency, and d_n is the line width of the resonance for quantum well n. An exemplary fit is shown in Figure 2e; good agreement with experimental results is achieved when eq 1 is combined with the continuum line shape.

Fractional quantum well concentrations are plotted as a function of milling depth in Figure 2f. The points at a depth of 0 nm represent the full-thickness film, whereas the depths of the milled regions are indicated on the horizontal axis. The data suggest that the concentrations of n = 3 quantum wells are essentially constant at milling depths down to 250 nm; however, the deviation from linear behavior in the 250-375 nm range reflects a decrease in concentration closer to the substrate. In contrast, the n = 1 and n = 2 concentrations are negligible at milling depths less than ~150 nm, whereas homogeneous distributions are suggested by the linear decrease in concentrations measured at greater depths. These data confirm that the quantum wells exhibit concentration gradients as suggested by earlier fluorescence data.²¹ The concentrations of larger quantum wells could not be determined in these films because the intensities of the resonances are comparable to or less than the noise level.

During milling experiments, there is potential for FIBinduced amorphization and deformation of the remaining perovskite film due to bombardment with high-energy Ga+ ions. FIB studies of crystalline metals and semiconductors, as well as polymer materials, estimate the Ga+ penetration depth at 20-60 nm when using a 30 kV accelerating voltage.³ Similar FIB milling experiments on thin polymer films³⁸ and perovskite solar cells³⁹ report structural changes at depths of 10 nm or less over the course of FIB milling. The absorbance spectra presented in Figure 2 suggest that the effects of FIBinduced amorphization are minimal because the signal depends on the full path length of the residual material. For example, the absorbance spectrum of a film at a milled depth of 380 nm (see Figure S4 in the Supporting Information) still exhibits excitonic resonances at the standard wavelengths and possesses a line shape similar to that of the full-thickness film.

The relative orientations of neighboring quantum wells have important implications for energy transfer efficiencies and optical properties. In an ideal coplanar geometry, the transition dipole coupling scales as the inverse square of the distance between quantum wells rather than the inverse cube when the quantum wells have infinite dimensions. Thus, it should not be assumed that the coupling scales as the inverse square of the distance between quantum wells if the orientations are random. In addition, the absorption coefficient for the film will depend on the angle of incidence if the transition dipole orientations are anisotropic.

The orientations of the quantum wells are investigated by collecting absorption spectra with p-polarized light at various angles of incidence.⁴¹ At an incidence angle of 0°, the electric field vector of the light source is in the plane of the film, whereas the projection of the electric field onto an axis normal to the film increases as the angle of incidence increases. Thus, the absorbance spectra will be sensitive to the angle of incidence if the transition dipoles are primarily in-plane or out-of-plane. The insensitivity of the absorbance spectra in Figure 3 to the angle of incidence suggests that the quantum wells

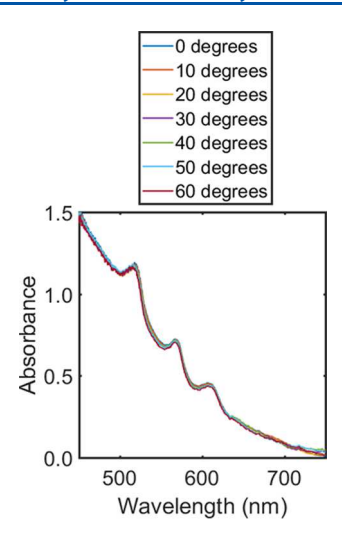


Figure 3. Absorbance spectra of layered perovskite film measured with p-polarized light are insensitive to the angle of incidence. This suggests that the quantum wells have random orientations.

have random orientations. The finding of quantum wells with random orientations is consistent with our assumption that the transition dipole coupling scales as the inverse cube of the distance between quantum wells in ref 21.

IIIB. Transient Absorption Spectra. The transient absorption spectra presented in Figure 4 are obtained by

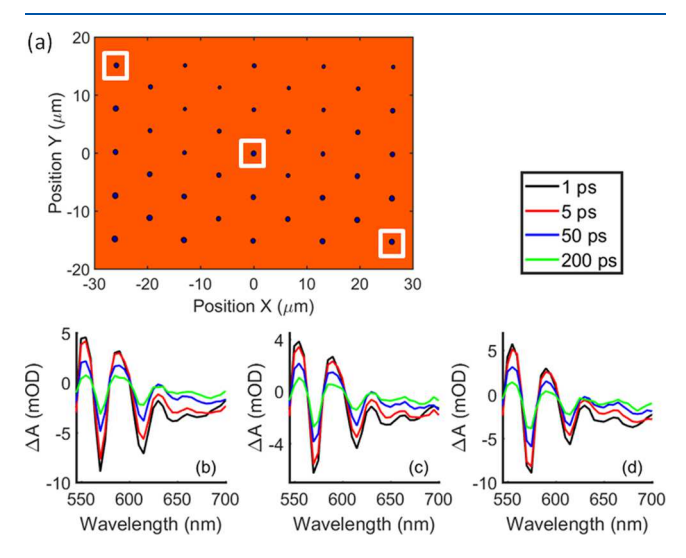


Figure 4. Transient absorption microscopy is conducted with a diffractive optic that produces 41 pump beams with $1.0 \, \mu m$ spot sizes. (a) The dynamics are imaged with a wide-field probe beam whose diameter is much larger than the field of view. (b)–(d) The transient absorption spectra of the films exhibit a progression of peaks with negative and positive signs, which represent single-exciton and single-to-biexciton transitions. The transient absorption line shapes vary little within the field of view for well-prepared films.

scanning the wavelength of a probe beam after excitation with 530 nm pump beams. The line shapes vary little within the field-of-view for well-prepared films, whereas the signal magnitudes typically vary by 10–20% at different spots. The 530 nm pump pulses are blue-shifted from the exciton resonances; however, each of the quantum wells absorbs light into higher-energy continuum states, as evidenced by the intense single-exciton resonances with negative signs at 570,

610, and 645 (n = 2, 3, and 4 quantum wells). In previous work, fits of transient absorption data for this system showed that the initial photoinduced population of the n = 2 quantum well is approximately 1.3 and 3.8 times larger than those of the n = 3 and 4 systems, respectively.²¹ The line widths of the resonances increase, and the signal has a negative sign at wavelengths greater than 650 nm. These aspects of the spectra at longer wavelengths reflect the loss of confinement and are consistent with the broad fluorescence spectra measured for the largest quantum wells in this system.²¹

The progression of peaks with positive and negative signs is understood by decomposing the signal into ground state bleach (GSB), excited state emission (ESE), and excited state absorption (ESA) nonlinearities.⁴² In previous work, we have shown that the dominant features of the spectra are fully captured with a model in which each quantum well is treated as a three-level system: ground, single-exciton, and biexciton states.²¹ Peaks with negative signs represent the single-exciton resonances in the GSB and ESE signal components. Each of the single-exciton transitions is accompanied by a single-tobiexciton resonance with a positive sign, which is associated with the ESA signal component. Notably, a similar progression of peaks with alternating signs has been assigned to a Stark effect induced by charge transfer excitons in perovskite nanoparticles; 43 transient absorption spectra are modeled by differentiating the linear absorbance spectra in this interpretation. Although peaks with alternating signs are obtained by differentiating the linear absorbance spectrum, this collective view of the nonlinear response conflicts with the predictions of time-dependent perturbation theory. 42 For example, the system evolves in a ground state population during the pump-probe delay in the GSB signal component. Therefore, the line shape of the GSB is insensitive to excited state dynamics and must enter the response function with a negative sign (ΔA < 0). The GSB should be distinguished from the ESE signal component, which may undergo a dynamic red shift due to energy and/or electron transfer processes. The magnitude of the ESE terms in the response function may also decay because of exciton dissociation, whereas the GSB signal component does not relax until the ground state is repopulated (i.e., the GSB and ESE can decay on different time scales). In contrast, the GSB and ESE become artificially entangled when transient absorption spectra are modeled by differentiating the linear absorbance spectrum to simulate a Stark effect.

We consider a Stark effect induced by charge transfer excitons to be unlikely in the present system for several reasons: (i) the resonance frequencies do not change within 1.5 ns after photoexcitation; ²¹ (ii) the dynamics of single and biexciton signal intensities are fully captured with coupled kinetic equations expressed in the single exciton basis; ^{21,22} (iii) confinement effects give rise to peaks with alternating signs in transient absorption spectra acquired for tightly bound excitonic systems such as molecular aggregates; 44,45 (iv) biexciton electronic states have been detected in layered 2D perovskites using a nonlinear optical technique designed to probe doubly excited states. 46 If a Stark effect contributes in the present systems, charge transfer excitons must form at interfaces on the sub-500 fs time scale and have no impact on the resonance frequencies or dynamics for the subsequent 1.5 ns (i.e., the charge transfer excitons must have lifetimes much longer than 1.5 ns). 43 For these reasons, we consider biexciton electronic structure to be the most plausible explanation for the

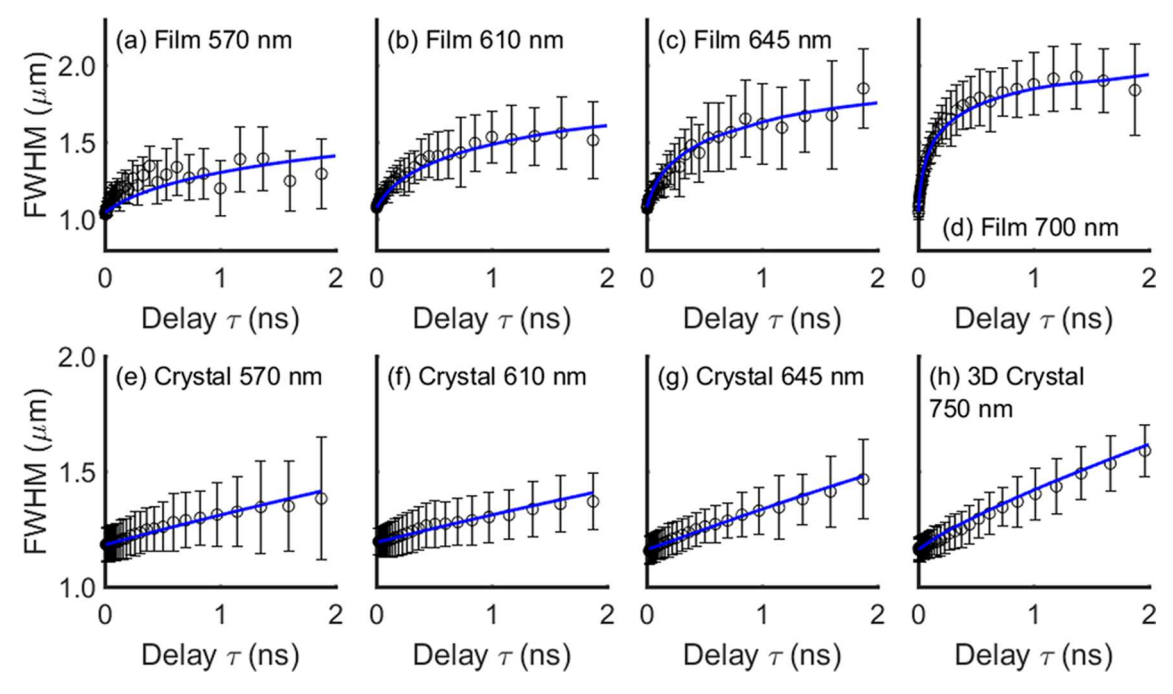


Figure 5. Spot widths are obtained by computing the averages (black points) and standard deviations (black bars) for 41 pump spots (the uncertainty ranges span 2 standard deviations). The averaged widths are fit with the diffusion equation (blue). Expansions of the signal spots in the film are dominated by two-body recombination, whereas the dynamics in the crystals are associated with diffusion.

signal components with positive signs in the transient absorption spectra.

In addition to energy transfer, we found that 40-50% of electronic excitations relax by way of "dark" nonradiative decay processes in each of the quantum wells.²¹ These "dark" decay processes, which enter the model in ref 21 by way of an overall decay in signal intensity, do not produce resonances in the visible spectral range and therefore cannot be assigned without ambiguity. The time scale of the decay is consistent with excited-state deactivation at "layer edge states"; 32 however, alternate exciton dissociation processes and/or charge transfer are possibilities. Further details regarding the fitting of transient absorption line shapes and extraction of rate constants from experimental data can be found in Reference.²¹

IIIC. Diffusion and Nonlinear Recombination Dynamics. TAM experiments are conducted on both layered perovskite films and phase-pure n = 2, 3, and 4 single crystals to understand the nature of the dynamics. This approach is motivated by previous work in which we found that the spot expansions in bulk perovskite crystals and films are dominated by diffusion and two-body recombination dynamics, respectively.²⁸ The widths of the signal spots are fit at each delay time to produce the full width half maxima displayed in Figure 5. In the film, signal detection at 570, 610, 645, and 700 nm corresponds to the n = 2, 3, 4, and 6 quantum wells, respectively. The error bars in these plots represent standard deviations in the widths computed for the 41 signal spots; these uncertainty ranges represent a combination of sample heterogeneity and experimental error. Fast acquisition of statistical information is one advantage of conducting 41 experiments in parallel. Of course, TAM instruments based on MHz laser systems can afford to raster scan individual laser beams while keeping data acquisition times manageable.²³⁻²⁷

The average values of the spot widths are fit with a diffusion equation as discussed in previous work,24

$$\frac{\partial N}{\partial \tau} = D_0 \frac{\partial^2 N}{\partial x^2} - \phi_2 N^2 \tag{2}$$

where x is a spatial coordinate, N is the carrier density, D_0 is a diffusion constant, and ϕ_2 describes two-body recombination. A single distribution, N, is used to describe electrons and holes because of their similar effective masses and spatial distributions. This equation does not include a firstorder term because it would not have an impact on the spot widths. If the initial distribution is Gaussian, then the widths will increase with the delay time but the distribution will remain Gaussian if ϕ_2 is set equal to zero. Two-body recombination produces a change in the spot widths that is unrelated to diffusion because the spatial distribution of N^2 is narrower than that of *N*.

The spot widths expand with the delay time in both films and crystals; however, the profiles, which are nearly linear in the crystals, exhibit a pronounced density dependence in the films. Similar behaviors were observed in a comparative study of bulk perovskite films and crystals.²⁸ Our analysis of those systems suggested that the dynamics are dominated by diffusion in the crystals, whereas two-body recombination processes induce spot expansions in the films. For this reason, we fit the profiles for the crystals with a single parameter, D_0 (i.e., ϕ_2 is set equal to zero because it induces curvature, whereas the experimental data points are linearly distributed). Similarly, the diffusion constants for the films are set equal to zero in these fits because the spot size expansions observed at delay times less than 500 ps are too fast for diffusion to be a physically reasonable interpretation; the diffusion constants of the films would be at least a factor of 10⁵ larger than those determined for the crystals. The behaviors of the films are qualitatively consistent with quasi-ballistic effects in that the magnitudes of the spot expansions increase as the difference between the photon energy of the pump and band gap increases. 47 However, the insensitivity of the spot widths to the

pump wavelength displayed in Figure 6 suggests that quasiballistic dynamics do not occur in this system. Therefore, the spot widths for the films are fit with the two-body recombination parameter, ϕ_{2} , alone.

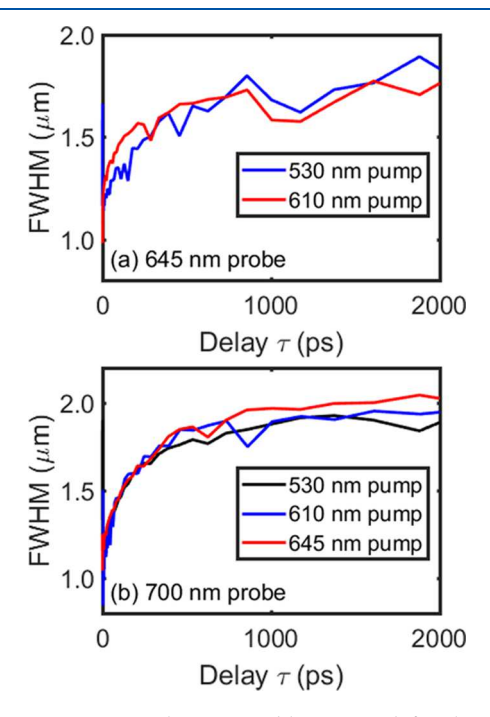


Figure 6. Dynamics in the spot width measured for the films are insensitive to the pump wavelength. (a) The n=4 quantum wells are probed at 645 nm following excitation at 530 and 610 nm. (b) The $n=\infty$ quantum wells are probed at 700 nm following excitation at 530, 610, and 645 nm. These data suggest that quasi-ballistic effects do not contribute to the dynamics in these systems. Rather, we assign the dynamics to a two-body recombination mechanism.

The fitting parameters are summarized in Figure 7 with standard deviations produced by conducting experiments on five separate samples. The two-body recombination parameters, ϕ_2 , determined for the films increase as the sizes of the quantum wells increase. For reference, the two-body recombination coefficients obtained for bulk perovskite films are approximately $3.3 \times 10^{-9} \text{ cm}^3/\text{s}$, which is in good agreement with values reported using alternate experimental methods (i.e., a range of $(0.8-20) \times 10^{-9} \text{ cm}^3/\text{s}$). We suggest that the trend in the ϕ_2 parameters displayed in Figure 7a represents an increase in the fraction of free charge carriers associated with a decrease in the exciton binding energies. The fraction of free charge carriers, f, may be estimated using the Saha equation,

$$\frac{f^2}{1-f} = \frac{1}{\rho} \left(\frac{2\pi m_{\text{eff}} k_{\text{B}} T}{h^2} \right)^{3/2} \exp \left(-\frac{E_{\text{b}}}{k_{\text{B}} T} \right)$$
(3)

where ρ is the excitation density, $m_{\rm eff}$ is the effective mass, and $E_{\rm b}$ is the binding energy. All parameters are given in Table 1. The percentages of free charge carriers computed for the n=2, 3, 4, and ∞ systems are 1.6, 3.1, 5.0, and 50%, respectively. The increase in the value of f with the size of the quantum well is consistent with our finding that the two-body recombination parameter increases with the size of the quantum well. That is, two-body recombination requires two particles that are most likely electrons and holes (i.e., not a pair of excitons). $^{52,58-60}$

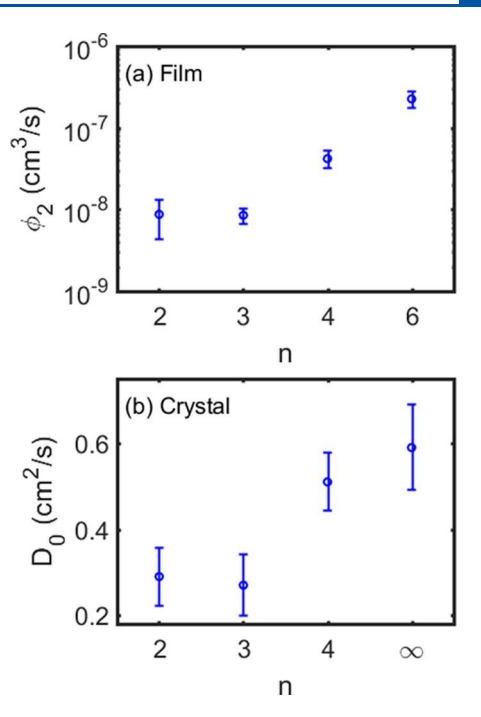


Figure 7. Different equations are used to fit spot widths obtained for (a) films and (b) single crystals. Two-body recombination and diffusion dominate in the film and crystal, respectively. The $n=\infty$ data point for the crystal is adapted from ref 28. The uncertainty ranges represent standard deviations computed for five separate samples.

While it is reasonable to use the Saha equation for the present densities, ⁶¹ it is possible that value of 50% computed for the $n = \infty$ system is underestimated due to limitations of the model.

The diffusion constants obtained for the single crystals, which are within the range of values previously reported for 3D perovskites (0.02–1.77 cm²/s), ^{26,28,47,51,55,62–64} vary by less than a factor of 3 and have overlapping error ranges (see Figure 7b). Therefore, we are reluctant to conclude that the larger quantum wells truly have larger diffusivities. It is possible that the larger diffusivities determined for the n = 4 and ∞ systems represent an increase in the fraction of free charge carriers. More importantly, the observation of diffusion in the crystals suggests that such dynamics are suppressed in the films. As in ref 28, we suggest that the presence of grain boundaries in the film promotes two-body recombination processes by confining the excitations to individual grains. While lateral motion of excitons and/or free charges is suppressed in the films, diffusion of excitations may still be possible from the glass to air sides of the films because the \sim 0.5 μ m film thickness is less than the \sim 1 μ m grain size.²¹

IV. CONCLUDING REMARKS

In summary, we have investigated the distribution of quantum well concentrations and spatial dynamics of electronic excitations in layered 2D perovskite films. The sizes of the quantum wells are shown to increase from the glass to air sides of the film, confirming the layering effect suggested by previous fluorescence data. This distribution of quantum well concentrations produces a gradient in excitation frequencies that facilitates a unidirectional energy transfer cascade (i.e., an energy funnel).

As in our earlier study of 3D perovskite systems, ²⁸ TAM experiments demonstrate that ultrafast dynamics are domi-

Table 1. Fraction of Free Charge Carriers Estimated for Quantum Wells

parameters ^{a,b}	n = 2	n = 3	n = 4	$n = \infty^c$
ρ (cm ⁻³)	2.94×10^{17}	1.15×10^{18}	9.13×10^{17}	7.58×10^{17}
$m_{\rm eff}/m_0^{\ a}$	0.217	0.201	0.196	0.104
$E_{\rm b}~({ m meV})$	251	177	157	2
f	0.016	0.031	0.050	0.504

 $^{{}^}am_0$ is the mass of a free electron. b Parameters of n=2, 3, and 4 quantum wells are from ref 31. c Parameters for $n=\infty$ are from ref 49 with the exception of E_b , which is taken from ref 50.

nated by diffusion and two-body recombination processes in single crystals and films, respectively. The diffusivities of the 2D systems are not remarkable in that they are within the range of values previously reported for the bulk system. The two-body recombination parameters increase with the sizes of the quantum well for systems with n > 3. This behavior is consistent with an increase in the fraction of free charge carriers with the size of the quantum well. The present work suggests that confinement of the charge carriers in the largest quantum wells enhances the two-body recombination rates as compared to the bulk perovskite film; the two-body recombination parameter obtained above for a quantum well with n = 6 (2.3 × 10⁻⁷ cm³/s) is close to 100 times larger than that determined using the same approach for the bulk perovskite $(3.3 \times 10^{-9} \text{ cm}^3/\text{s}).^{28}$ Together with larger transition dipoles, the enhancement of two-body effects in the quantum wells with n > 4 suggests that the spontaneous emission rate will be much greater in the 2D systems as compared to the bulk.52

It has been established that bulk perovskites constitute effective gain media for microcavity lasers because of large oscillator strengths, long excited-state lifetimes, and large twobody recombination rates. 58,65 Of course, confinement of excitations in 2D quantum wells supports even larger oscillator strengths and exciton binding energies. In addition, the present work suggests that two-body recombination processes will also be enhanced in films composed of 2D quantum wells with n > 14. Knowledge of how such two-body recombination processes vary with the sizes of the quantum wells may hold implications for the function of microcavity lasers based on layered 2D perovskite systems. Recent work on lead-bromide layered perovskites suggests that the energy funneling functionality of layered 2D perovskite systems may promote population inversion in the larger, quasi-3D quantum wells.⁶⁶ These results are consistent with the present work in that microcavity lasing was found to be most efficient in quantum wells with n > 1

ASSOCIATED CONTENT

S Supporting Information

The Supporting Information is available free of charge at https://pubs.acs.org/doi/10.1021/acs.jpca.9b08852.

Model used to estimate carrier densities is described, tables of spectral fitting parameters, FIB milling results summarized for individual samples (SEM images, absorption data, quantum well concentration vs milling depth), AFM depth profiles, linear absorbance spectra for perovskite single crystals (PDF)

AUTHOR INFORMATION

Corresponding Author

*ammoran@email.unc.edu.

ORCID ®

Jun Hu: 0000-0002-6997-0174 Wei You: 0000-0003-0354-1948

Andrew M. Moran: 0000-0001-7761-7613

Notes

The authors declare no competing financial interest.

ACKNOWLEDGMENTS

This work is supported by the National Science Foundation under CHE-1763207 (O.F.W., N.Z., Z.O., and A.M.M.) and DMR-1610879 (J.H. and W.Y.). FIB milling tests were conducted at the Chapel Hill Analytical and Nanofabrication Laboratory, CHANL, a member of the North Carolina Research Triangle Nanotechnology Network, RTNN, which is supported by the National Science Foundation, Grant ECCS-1542015, as part of the National Nanotechnology Coordinated Infrastructure, NNCI.

REFERENCES

- (1) Kojima, A. T. K; Shirai, Y.; Miyasaka, T. Organometal Halide Perovskites as Visible-Light Sensitizers for Photovoltaic Cells. *J. Am. Chem. Soc.* **2009**, *131*, 6050–6051.
- (2) Lee, M. M. T. J.; Miyasaka, T.; Murakami, T. N.; Snaith, H. J. Efficient Hybrid Solar Cells Based on Meso-Superstructured Organometal Halide Perovskites. *Science* **2012**, *338*, 643–647.
- (3) Kim, H. S.; Lee, C. R.; Im, J. H.; Lee, K. B.; Moehl, T.; Marchioro, A.; Moon, S. J.; Humphry-Baker, R.; Yum, J. H.; Moser, J. E.; et al. Lead iodide perovskite sensitized all-solid-state submicron thin film mesoscopic solar cell with efficiency exceeding 9%. *Sci. Rep.* **2012**, *2*, 591.
- (4) Smith, I. C.; Hoke, E. T.; Solis-Ibarra, D.; McGehee, M. D.; Karunadasa, H. I. A Layered Hybrid Perovskite Solar-Cell Absorber with Enhanced Moisture Stability. *Angew. Chem., Int. Ed.* **2014**, *53*, 11232–11235.
- (5) Zhang, X.; Ren, X.; Liu, B.; Munir, R.; Zhu, X.; Yang, D.; Li, J.; Liu, Y.; Smilgies, D.-M.; Li, R.; et al. Stable high efficiency two-dimensional perovskite solar cells via cesium doping. *Energy Environ. Sci.* **2017**, *10*, 2095–2102.
- (6) Ke, W.; Mao, L.; Stoumpos, C. C.; Hoffman, J.; Spanopoulos, I.; Mohite, A. D.; Kanatzidis, M. G. Compositional and Solvent Engineering in Dion-Jacobson 2D Perovskites Boosts Solar Cell Efficiency and Stability. *Adv. Energy Mater.* **2019**, *9*, 1803384.
- (7) Ishihara, T.; Takahashi, J.; Goto, T. Exciton-State in Two-Dimensional Perovskite Semiconductor $(C_{10}H_{21}NH_3)_2PbI_4$. Solid State Commun. 1989, 69, 933–936.
- (8) Ishihara, T.; Takahashi, J.; Goto, T. Optical-Properties Due to Electronic-Transitions in 2-Dimensional Semiconductors $(C_nH_{2n+1}NH_3)_2PbI_4$. Phys. Rev. B: Condens. Matter Mater. Phys. 1990, 42, 1109–11107.
- (9) Calabrese, J.; Jones, N. L.; Harlow, R. L.; Herron, N.; Thorn, D. L.; Wang, Y. Preparation and Characterization of Layered Lead Halide Compounds. J. Am. Chem. Soc. 1991, 113, 2328–2330.
- (10) Hong, X.; Ishihara, T.; Nurmikko, A. V. Dielectric Confinement Effect on Excitons in PbI₄-Based Layered Semiconductors. *Phys. Rev. B: Condens. Matter Mater. Phys.* **1992**, *45*, 6961–6964.

- (11) Smith, I. C.; Hoke, E. T.; Solis-Ibarra, D.; Mcgehee, M. D.; Karunadasa, H. I. A Layered Hybrid Perovskite Solar-Cell Absorber with Enhanced Moisture Stability. *Angew. Chem., Int. Ed.* **2014**, 53, 11232–11235.
- (12) Yuan, M.; Quan, L. N.; Comin, R.; Walters, G.; Sabatini, R.; Voznyy, O.; Hoogland, S.; Zhao, Y.; Beauregard, E. M.; Kanjanaboos, P.; et al. Perovskite Energy Funnels for Efficient Light-Emitting Diodes. *Nat. Nanotechnol.* **2016**, *11*, 872–877.
- (13) Wang, N.; Cheng, L.; Ge, R.; Zhang, S.; Miao, Y.; Zou, W.; Yi, C.; Sun, Y.; Cao, Y.; Yang, R.; et al. Perovskite Light-Emitting Diodes Based on Solution-Processed Self-Organized Multiple Quantum Wells. *Nat. Photonics* **2016**, *10*, 699–704.
- (14) Stoumpos, C. C.; Cao, D. H.; Clark, D. J.; Young, J.; Rondinelli, J. M.; Jang, J. I.; Hupp, J. T.; Kanatzidis, M. G. Ruddlesden—Popper Hybrid Lead Iodide Perovskite 2D Homologous Semiconductors. *Chem. Mater.* **2016**, 28, 2852–2867.
- (15) Katan, C.; Mercier, N.; Even, J. Quantum and Dielectric Confinement Effects in Lower-Dimensional Hybrid Perovskite Semiconductors. *Chem. Rev.* **2019**, *119*, 3140–3192.
- (16) Hu, J.; You, W. Two-Dimensional Organic—Inorganic Hybrid Perovskites: A New Platform for Optoelectronic Applications. *Adv. Mater.* **2018**, *30*, e1082041.
- (17) Zaslow, B.; Zandler, M. E. Two-Dimensional Analog to the Hydrogen Atom. Am. J. Phys. 1967, 35, 1118–1119.
- (18) Yang, X. L.; Guo, S. H.; Chan, F. T.; Wong, K. W.; Ching, W. Y. Analytic Solution of a Two-Dimensional Hydrogen Atom. I. Nonrelativistic Theory. *Phys. Rev. A: At., Mol., Opt. Phys.* **1991**, 43, 1186–1196.
- (19) Yu, P. Y.; Cardona, M. Fundamentals of Semiconductors: Physics and Materials Properties, Fourth ed.; Springer: New York, 2010.
- (20) Liu, J.; Leng, J.; Wu, K.; Zhang, J.; Jin, S. Observation of Internal Photoinduced Electron and Hole Separation in Hybrid Two-Dimensional Perovskite Films. *J. Am. Chem. Soc.* **2017**, *139*, 1432–1435
- (21) Williams, O. F.; Guo, Z.; Hu, J.; Yan, L.; You, W.; Moran, A. M. Energy Transfer Mechanisms in Layered 2D Perovskites. *J. Chem. Phys.* **2018**, *148*, 134706.
- (22) Yan, L.; Hu, J.; Guo, Z.; Chen, H.; Toney, M. F.; Moran, A. M.; You, W. Synthetic Control Over Orientational Degeneracy of Spacer Cations Enhances Solar Cell Efficiency in Two-Dimensional Perovskites. ACS Appl. Mater. Interfaces 2018, 10, 33187–33197.
- (23) Wong, C. Y.; Penwell, S. B.; Cotts, B. L.; Noriega, R.; Wu, H.; Ginsberg, N. S. Revealing Exciton Dynamics in a Small-Molecule Organic Semiconducting Film with Subdomain Transient Absorption Microscopy. *J. Phys. Chem. C* **2013**, *117*, 22111–22122.
- (24) Gabriel, M. M.; Grumstrup, E. M.; Kirschbrown, J. R.; Pinion, C. W.; Christesen, J. D.; Zigler, D. F.; Cating, E. M.; Cahoon, J. F.; Papanikolas, J. M. Imaging Charge Separation and Carrier Recombination in Nanowire p-i-n Junctions Using Ultrafast Microscopy. *Nano Lett.* **2014**, *14*, 3079–3087.
- (25) Dong, Q.; Fang, Y.; Shao, Y.; Mulligan, P.; Qiu, J.; Cao, L.; Huang, J. Electron-Hole Diffusion Lengths > 175 μ m in Solution-Grown CH₃NH₃PbI₃ single crystals. *Science* **2015**, 347, 967–970.
- (26) Hill, A. H.; Smyser, K. E.; Kennedy, C. L.; Massaro, E. S.; Grumstrup, E. M. Screened Charge Carrier Transport in Methylammonium Lead Iodide Perovskite Thin Films. *J. Phys. Chem. Lett.* **2017**, *8*, 948–953.
- (27) Johns, P.; Yu, K.; Devadas, M. S.; Hartland, G. V. Role of Resonances in the Transmission of Surface Plasmon Polaritons between Nanostructures. *ACS Nano* **2016**, *10*, 3375–3381.
- (28) Guo, Z.; Zhou, N.; Williams, O. F.; Hu, J.; You, W.; Moran, A. M. Imaging Carrier Diffusion in Perovskites with a Diffractive Optic-Based Transient Absorption Microscope. *J. Phys. Chem. C* **2018**, *122*, 10650–10656.
- (29) Hill, A. H.; Kennedy, C. L.; Massaro, E. S.; Grumstrup, E. M. Perovskite Carrier Transport: Disentangling the Impacts of Effective Mass and Scattering Time Through Microscopic Optical Detection. *J. Phys. Chem. Lett.* **2018**, *9*, 2808–2813.

- (30) Steves, M. A.; Zheng, H.; Knappenberger, K. L. Correlated Spatially Resolved Two-Dimensional Electronic and Linear Absorption Spectroscopy. *Opt. Lett.* **2019**, *44*, 2117–2120.
- (31) Blancon, J.-C.; Stier, A. V.; Tsai, H.; Nie, W.; Stoumpos, C. C.; Traoré, B.; Pedesseau, L.; Kepenekian, M.; Katsutani, F.; Noe, G. T.; et al. Scaling Law for Excitons in 2D Perovskite Quantum Wells. *Nat. Commun.* **2018**, *9*, 2254.
- (32) Blancon, J.-C.; Tsai, H.; Nie, W.; Stoumpos, C. C.; Pedesseau, L.; Katan, C.; Kepenekian, M.; Soe, C. M. M.; Appavoo, K.; Sfeir, M. Y.; et al. Extremely Efficient Internal Exciton Dissociation Through Edge States in Layered 2D Perovskites. *Science* **2017**, 355, 1288–1292.
- (33) Wu, X.; Trinh, M. T.; Zhu, X. Y. Excitonic Many-Body Interactions in Two-Dimensional Lead Iodide Perovskite Quantum Wells. J. Phys. Chem. C 2015, 119, 14714–14721.
- (34) Raghavan, C. M.; Chen, T. P.; Li, S. S.; Chen, W. L.; Lo, C. Y.; Liao, Y. M.; Haider, G.; Lin, C. C.; Chen, C. C.; Sankar, R.; et al. Low-Threshold Lasing from 2D Homologous Organic-Inorganic Hybrid Ruddlesden-Popper Perovskite Single Crystals. *Nano Lett.* **2018**, *18*, 3221–3228.
- (35) Kim, C.-S.; Ahn, S.-H.; Jang, D.-Y. Review: Developments in Micro/Nanoscale Fabrication by Focused Ion Beams. *Vacuum* **2012**, *86*, 1014–1035.
- (36) Grumstrup, E. M.; Chen, Z.; Vary, R. P.; Moran, A. M.; Schanze, K. S.; Papanikolas, J. P. Frequency Modulated Femtosecond Stimulated Raman Spectroscopy of Ultrafast Energy Transfer in a Donor—Acceptor Copolymer. *J. Phys. Chem. B* **2013**, *117*, 8245—8255.
- (37) Fang, F.; Xu, Z. State-of-the-Art for Nanomanufacturing Using Ion-Beam Technology. *Handbook of Manufacturing Engineering and Technology*; Springer, 2013; pp 1–31.
- (38) Kim, S.; Jeong Park, M.; Balsara, N. P.; Liu, G.; Minor, A. M. Minimization of focused ion beam damage in nanostructured polymer thin films. *Ultramicroscopy* **2011**, *111*, 191–199.
- (39) Wang, S.; Sina, M.; Parikh, P.; Uekert, T.; Shahbazian, B.; Devaraj, A.; Meng, Y. S. Role of 4-tert-Butylpyridine as a Hole Transport Layer Morphological Controller in Perovskite Solar Cells. *Nano Lett.* **2016**, *16*, 5594–5600.
- (40) Tomita, A.; Shah, J.; Knox, R. S. Efficient Exciton Energy Transfer Between Widely Separated Quantum Wells at Low Temperatures. *Phys. Rev. B: Condens. Matter Mater. Phys.* **1996**, 53, 10793–10803.
- (41) Moran, A. M.; Sung, J.; Hicks, E. M.; Van Duyne, R. P.; Spears, K. G. Second Harmonic Excitation Spectroscopy of Silver Nanoparticle Arrays. *J. Phys. Chem. B* **2005**, *109*, 4501–4506.
- (42) Mukamel, S. Principles of Nonlinear Optical Spectroscopy; Oxford University Press: New York, 1995.
- (43) Bouduban, M. E. F.; Burgos-Caminal, A.; Ossola, R.; Teuscher, J.; Moser, J. E. Energy and Charge Transfer Cascade in Methylammonium Lead Bromide Perovskite Nanoparticle Aggregates. *Chem. Sci.* **2017**, *8*, 4371–4380.
- (44) Fidder, H.; Knoester, J.; Wiersma, D. A. Observation of the one-exciton to two-exciton transition in a J aggregate. *J. Chem. Phys.* **1993**, *98*, *6564–6566*.
- (45) Sperling, J.; Nemeth, A.; Hauer, J.; Abramavicius, D.; Mukamel, S.; Kauffmann, H. F.; Milota, F. Excitons and Disorder in Molecular Nanotubes: A 2D Electronic Spectroscopy Study and First Comparison to a Microscopic Model. *J. Phys. Chem. A* **2010**, *114*, 8179–8189.
- (46) Elkins, M. H.; Pensack, R.; Proppe, A. H.; Voznyy, O.; Quan, L. N.; Kelley, S. O.; Sargent, E. H.; Scholes, G. D. Biexciton Resonances Reveal Exciton Localization in Stacked Perovskite Quantum Wells. *J. Phys. Chem. Lett.* **2017**, *8*, 3895–3901.
- (47) Guo, Z.; Wan, Y.; Yang, M.; Snaider, J.; Zhu, K.; Huang, L. Long-Range Hot-Carrier Transport in Hybrid Perovskites Visualized by Ultrafast Microscopy. *Science* **2017**, *356*, 59–62.
- (48) Gélvez-Rueda, M. C.; Hutter, E. M.; Cao, D. H.; Renaud, N.; Stoumpos, C. C.; Hupp, J. T.; Savenije, T. J.; Kanatzidis, M. G.; Grozema, F. C. Interconversion Between Free Charges and Bound

- Excitons in 2D Hybrid Lead Halide Perovskites. *J. Phys. Chem. C* **2017**, 121, 26566–26574.
- (49) Miyata, A.; Mitioglu, A.; Plochocka, P.; Portugall, O.; Wang, J. T.-W.; Stranks, S. D.; Snaith, H. J.; Nicholas, R. J. Direct Measurement of the Exciton Binding Energy and Effective Masses for Charge Carriers in Organic-Inorganic Tri-Halide Perovksites. *Nat. Phys.* **2015**, *11*, 582–588.
- (50) Lin, Q.; Armin, A.; Nagiri, R. C. R.; Burn, P. L.; Meredith, P. Electro-Optics of Perovskite Solar Cells. *Nat. Photonics* **2015**, *9*, 106–112.
- (51) Savenije, T. J.; Ponseca, C. S.; Kunneman, L.; Abdellah, M.; Zheng, K.; Tian, Y.; Zhu, Q.; Canton, S. E.; Scheblykin, I. G.; Pullerits, T.; et al. Thermally Activated Exciton Dissociation and Recombination Control the Carrier Dynamics in Organometal Halide Perovskites. J. Phys. Chem. Lett. 2014, 5, 2189–2194.
- (52) Yamada, Y.; Nakamura, T.; Endo, M.; Wakamiya, A.; Kanemitsu, Y. Photocarrier Recombination Dynamics in Perovskite CH₃NH₃PbI₃ for Solar Cell Applications. *J. Am. Chem. Soc.* **2014**, *136*, 11610–11613.
- (53) Manser, J. S.; Kamat, P. V. Band Filling with Free Charge Carriers in Organometal Halide Perovskites. *Nat. Photonics* **2014**, *8*, 737–743.
- (54) D'Innocenzo, V.; Kandada, A. R. S.; De Bastiani, M.; Gandini, M.; Petrozza, A. Tuning the Light Emission Properties by Band Gap Engineering in Hybrid Lead Halide Perovskite. *J. Am. Chem. Soc.* **2014**, *136*, 17730.
- (55) Guo, Z.; Manser, J. S.; Wan, Y.; Kamat, P. V.; Huang, J. Spatial and Temporal Imaging of Long-Range Charge Transport in Perovskite Thin Film by Ultrafast Microscopy. *Nat. Commun.* **2015**, *6*, 7471.
- (56) Trinh, M. T.; Wu, X.; Niesner, D.; Zhu, X. Many-Body Interactions in Photoexcited Lead Iodide Perovskite. *J. Mater. Chem.* A **2015**, 3, 9285–9290.
- (57) Herz, L. M. Charge-Carrier Dynamics in Organic-Inorganic Metal Halid Perovskites. *Annu. Rev. Phys. Chem.* **2016**, *67*, *65*–89.
- (58) Stranks, S. D.; Burlakov, V. M.; Leijtens, T.; Ball, J. M.; Goriely, A.; Snaith, H. J. Recombination Kinetics in Organic-Inorganic Perovskites: Excitons, Free Charge, and Subgap States. *Phys. Rev. Appl.* **2014**, 2, 034007.
- (59) Manser, J. S.; Kamat, P. V. Band filling with free charge carriers in organometal halide perovskites. *Nat. Photonics* **2014**, *8*, 737–743.
- (60) Yamada, Y.; Yamada, T.; Phuong, L. Q.; Maruyama, N.; Nishimura, H.; Wakamiya, A.; Murata, Y.; Kanemitsu, Y. Dynamic Optical Properties of CH₃NH₃PbI₃ Single Crystals As Revealed by One- and Two-Photon Excited Photoluminescence Measurements. *J. Am. Chem. Soc.* **2015**, *137*, 10456–10459.
- (61) Saba, M.; Cadelano, M.; Marongiu, D.; Chen, F.; Sarritzu, V.; Sestu, N.; Figus, C.; Aresti, M.; Piras, R.; Lehmann, A. G.; et al. Correlated Electron-Hole Plasma in Organometal Perovskites. *Nat. Commun.* **2014**, *5*, 5049.
- (62) Stranks, S. D.; Eperon, G. E.; Grancini, G.; Menelaou, C.; Alcocer, M. J. P.; Leijtens, T.; Herz, L. M.; Petrozza, A.; Snaith, H. J. Electron-Hole Diffusion Lengths Exceeding 1 Micrometer in an Organometal Trihalide Perovskite Absorber. *Science* **2013**, 342, 341–344.
- (63) Xing, G.; Mathews, N.; Sun, S.; Lim, S. S.; Lam, Y. M.; Grätzel, M.; Mhaisalkar, S.; Sum, T. C. Long-Range Balanced Electron- and Hole-Transport Lengths in Organic-Inorganic CH₃NH₃PbI₃. *Science* **2013**, 342, 344–347.
- (64) Tian, W.; Zhao, C.; Leng, J.; Cui, R.; Jin, S. Visualizing Carrier Diffusion in Individual Single-Crystal Organolead Halide Perovskite Nanowires and Nanoplates. *J. Am. Chem. Soc.* **2015**, *137*, 12458–12461.
- (65) Deschler, F.; Price, M.; Pathak, S.; Klintberg, L. E.; Jarausch, D.-D.; Higler, R.; Hüttner, S.; Leijtens, T.; Stranks, S. D.; Snaith, H. J.; et al. High Photoluminescence Efficiency and Optically Pumped Lasing in Solution-Processed Mixed Halide Perovskite Semiconductors. J. Phys. Chem. Lett. 2014, 5, 1421–1426.

(66) Zhang, H.; Liao, Q.; Wu, Y.; Zhang, Z.; Gao, Q.; Liu, P.; Li, M.; Yao, J.; Fu, H. 2D Ruddlesden-Popper Perovskites Microring Laser Array. *Adv. Mater.* **2018**, *30*, 1706186.